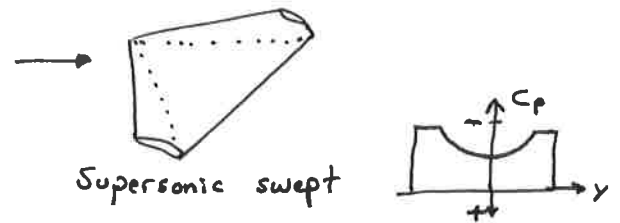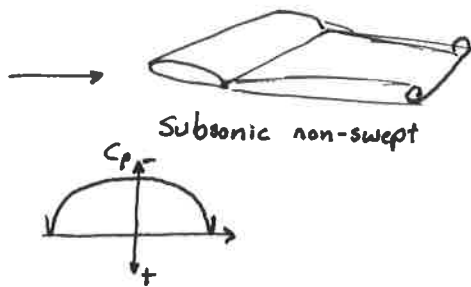Lesson 29

High AOA + LEX

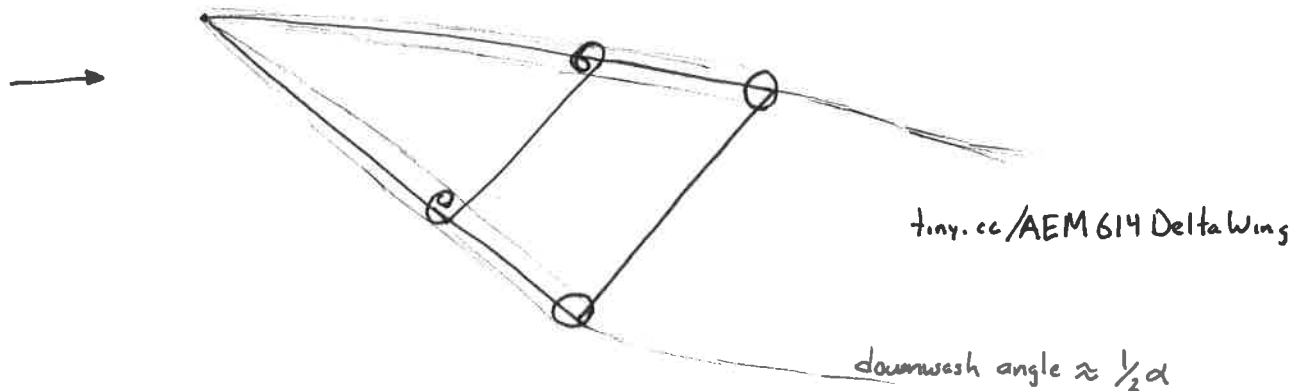# Slender Delta Wings in subsonic flow

Behavior is different from higher AR or rectangular non-swept planforms.

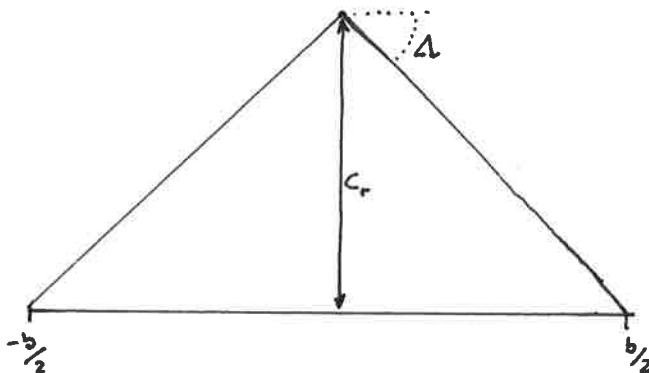Subsonic non-swept

Supersonic swept

As the LE sweep angle increases in a subsonic flow, a change in the flow occurs.

Leading edge vorticies form along the leading edge.

tiny.cc/AEM 614 DeltaWing

downwash angle $\approx \frac{1}{2}\alpha$
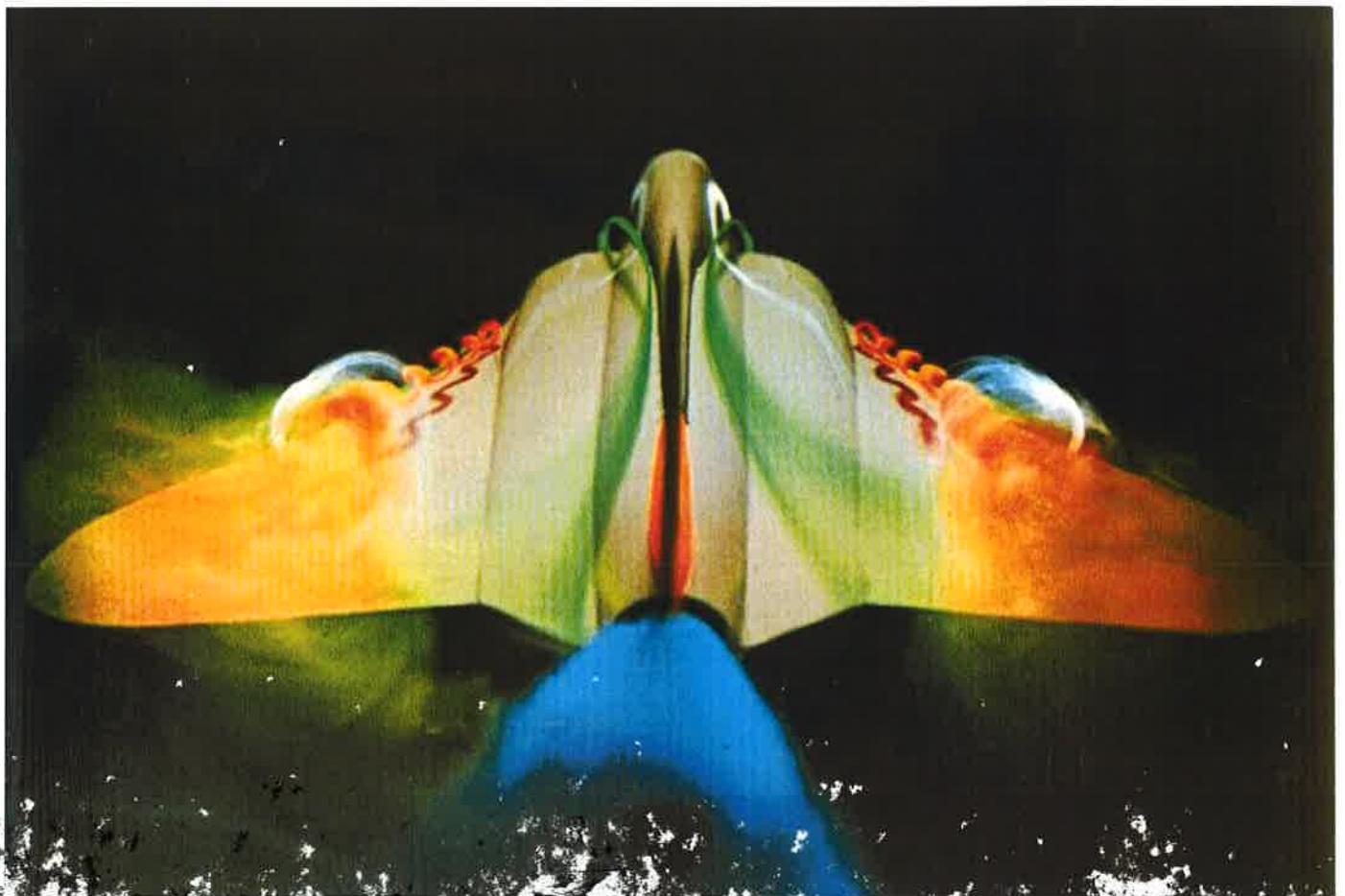
Geometry

$$\lambda = 0$$

$$\tan \Lambda = \frac{C_r}{b/2} \quad \text{and} \quad S = \frac{b \cdot C_r}{2}$$

$$AR = \frac{b^2}{S} = \frac{b^2}{b C_r \frac{1}{2}} = \frac{b^2}{b \, b \frac{1}{2} \tan \Lambda \frac{1}{2}}$$

$$\boxed{AR = \frac{4}{\tan \Lambda}}$$

Leading Edge Vorticies used to increase effective AOA range of aircraft.

Leading Edge Vorticies used to increase effective AOA range of aircraft.

2D Flow Approximation

C.P.
Cut plane
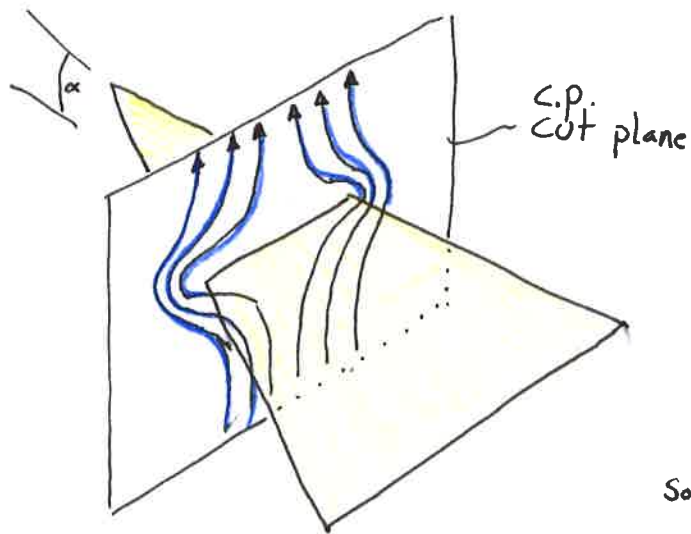
Source: McCormick 1995

The normal component of velocity is $V\alpha^{[rad]}$. The cut plane flow geometry is self similar and follows a velocity potential gov' equ.

$$\frac{\partial^2 \emptyset}{\partial y^2} + \frac{\partial^2 \emptyset}{\partial z^2} = 0 \quad \text{on the C.P.}$$

You should be thinking the following:
- Potential functions have no drag and no separation.
- Thus, the lift should be zero!! But the lift isn't zero!

Although the C.P. shape is self similar, the actual wing increases width as the flow moves from ~~apex~~ vertex to trailing edge. An increasing amount of fluid is being affected, so lift (being a momentum term derivative wrt time) is non zero.

Another way to view this process is that the potential flow "trapped" or "slowed" the equal time spacing along streamlines. There is an "apparent mass" associated with this operation.
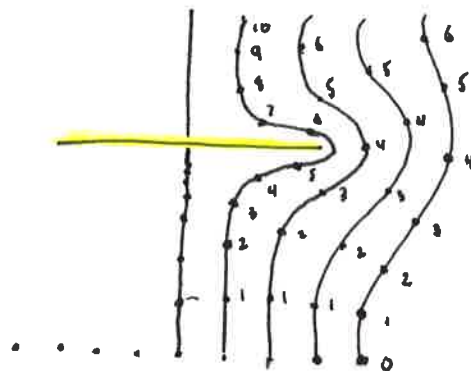
Not all particles exit the given domain in equal time.

The C.p. lift component is equal to the C.p. velocity $V\alpha$ and multiplied by the change in apparent mass.

$$L' = V\alpha \frac{dm'}{dt} \qquad \text{reminds of } F = \frac{d}{dt}(mV)$$

But $\frac{dm'}{dt} = \frac{dm'}{dx}\frac{dx}{dt} = V\frac{dm'}{dx}$

$$L' = V^2\alpha \frac{dm'}{dx}$$

The apparent mass in the C.p. is

$$m' = \pi \frac{b^2}{4}\rho\,dx \quad \Rightarrow \quad \frac{dm'}{dx} = \pi \frac{b^2}{4}\rho\,dx\,\underbrace{\frac{db}{dx}}_{\text{how does span increase with } x.}$$

The local lift coefficient is (after reduction)
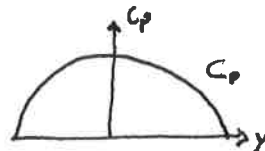
$$C_\ell = \pi\alpha \frac{db}{dx}$$

This gives (for a flat wing)

$$\Delta p = \frac{1}{2}\rho V^2 \cdot \frac{2\alpha}{\sqrt{1 - \left(\frac{2y}{b(x)}\right)^2}} \cdot \frac{db(x)}{dx}$$

Converting to a conical coordinate system, $\sin\theta = \sqrt{1 - \left(\frac{2y}{b}\right)^2}$

$$\frac{\Delta p}{8} = \frac{2\alpha}{\sin\theta}\frac{db}{dx}$$

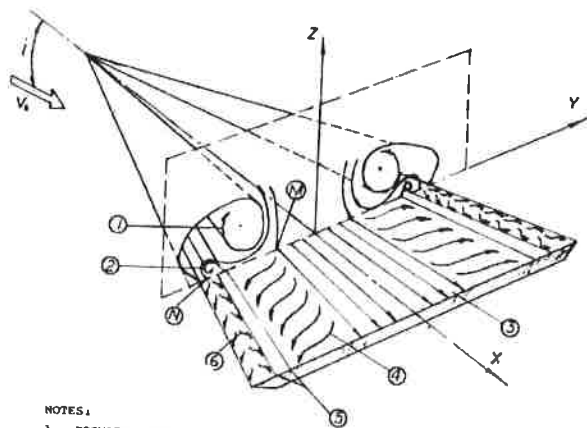This gives an elliptical spanwise loading !

$$C_{L\alpha} = \frac{\pi A}{2}$$

$$C_{D_i} = \frac{C_L^2}{\pi A}$$

This analysis is good for small angles and small AR.
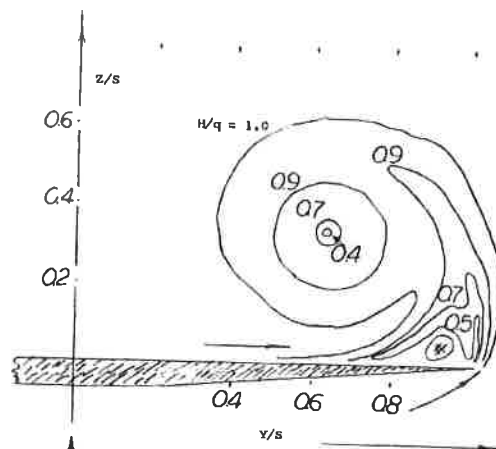
$$\alpha < 2 - 3° \qquad\qquad AR < 0.5$$

Actual Delta Wings create vorticies along the LE.

NOTES:
1. PRIMARY LEADING-EDGE VORTEX
2. SECONDARY VORTEX
3. AXIAL FLOW INBOARD ON WING SURFACE
4. LATERAL FLOW
5. TRANSITION
6. TIP FLOW

Figure 3. Flow distribution of a sharp-edge delta wing showing primary and secondary leading-edge vortices.

The vorticies are regions of low pressure occurring only on the upper surface.
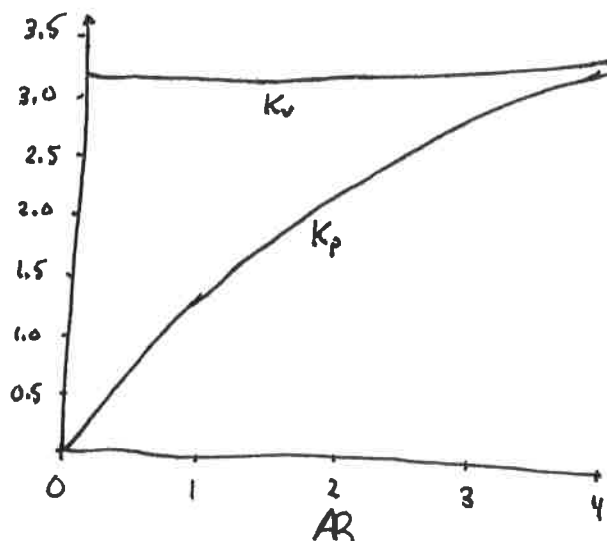
In 2D, the flow pattern is

Vortex lift is produced from the leading edge suction

Polhamus (NASA TN D-3767) provides

$$C_L = \underbrace{K_p \sin\alpha \cos^2\alpha}_{\substack{\text{potential flow lift} \\ \text{prev. page}}} + \underbrace{K_v \cos\alpha \sin^2\alpha}_{\text{separated vortex lift}}$$

$$CD = CDo + Kp \cdot \sin(\alpha)^2 \cdot \cos(\alpha) + Kv \cdot \sin(\alpha)^3$$

$$K_p = C_{L_\alpha} \text{ lifting Surface theory}$$
$$\frac{\pi A}{2}$$

$$K_v = \frac{K_p - K_p^2 K_i}{\cos \Lambda}$$

$$K_i = \frac{1}{\pi A}$$
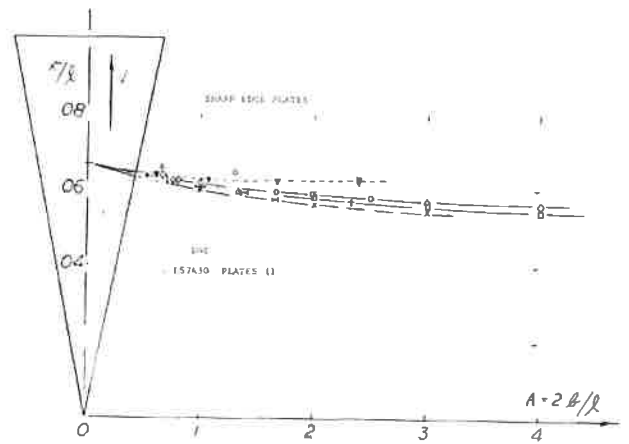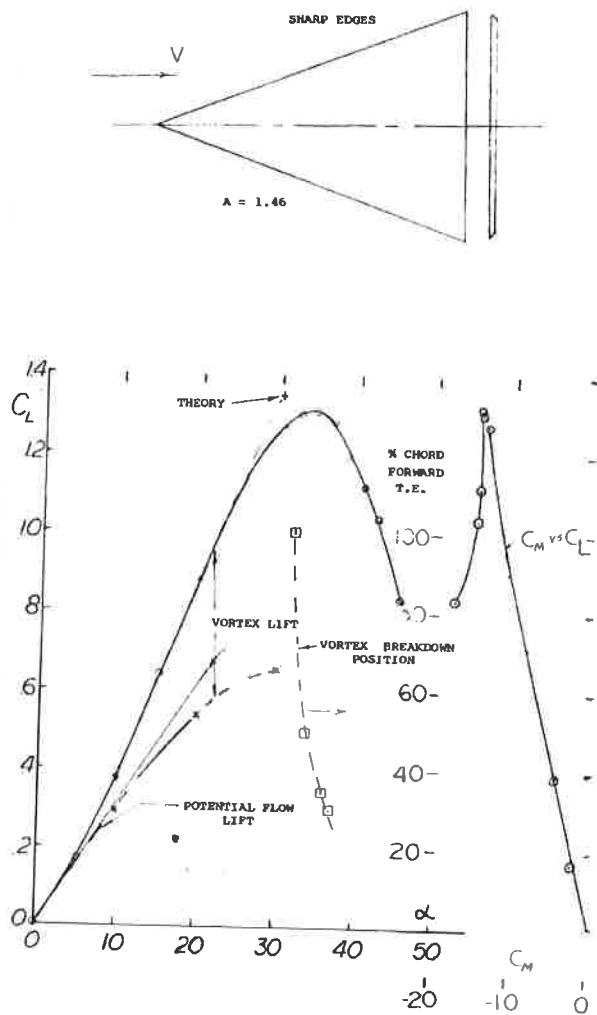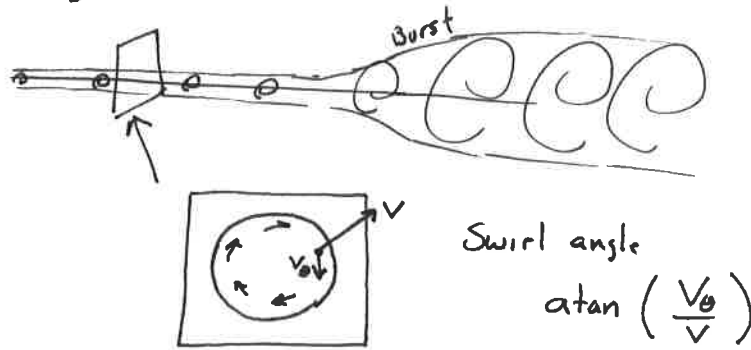
Aerodynamic Force Analysis

Figure 12. Aerodynamic center of delta wings derived from experimental results.

The a.c. is theoretically at $\frac{2}{3}c$ for $AR \approx 0$.

Vortex lift provides the majority of C_L as α increases beyond $20°$ (depending on configuration)

Vortex Bursting

Swirl angle

$$\mathrm{atan}\left(\frac{V_\theta}{V}\right)$$

When the swirl angle is large, an instability forms with the result of a significantly larger size and a lower swirl velocity. This is the vortex equivalent of hydraulic jump in an open channel or a shock in supersonic fluid.

Vortex bursting is troublesome for designers. The burst point is sensitive to design parameters and operational parameters.
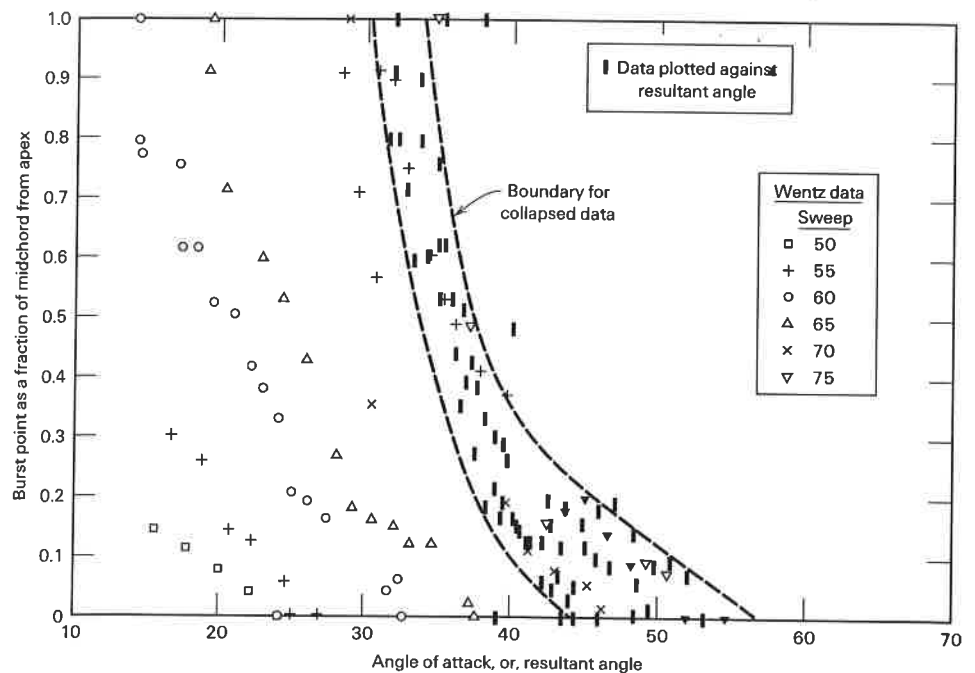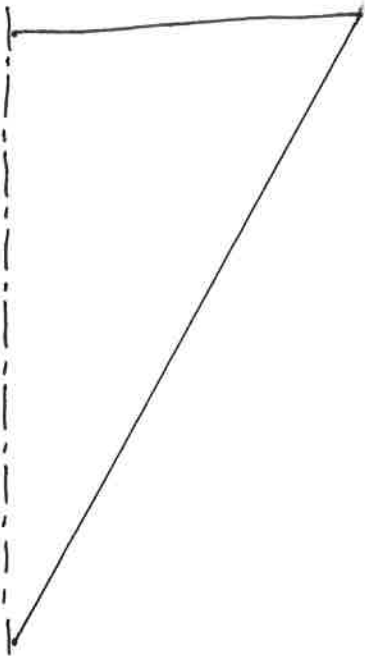

Figure 3.76 Burst point data as a function of angle of attack and resultant angle.

Vortex Bursting

The F-18 had a significant development issue with the LEX stroke vortex bursting and interacting with the canted verticles. The vortex created large stresses and eventually fatigue issues.

tiny.cc/AEM614 F18 HARV
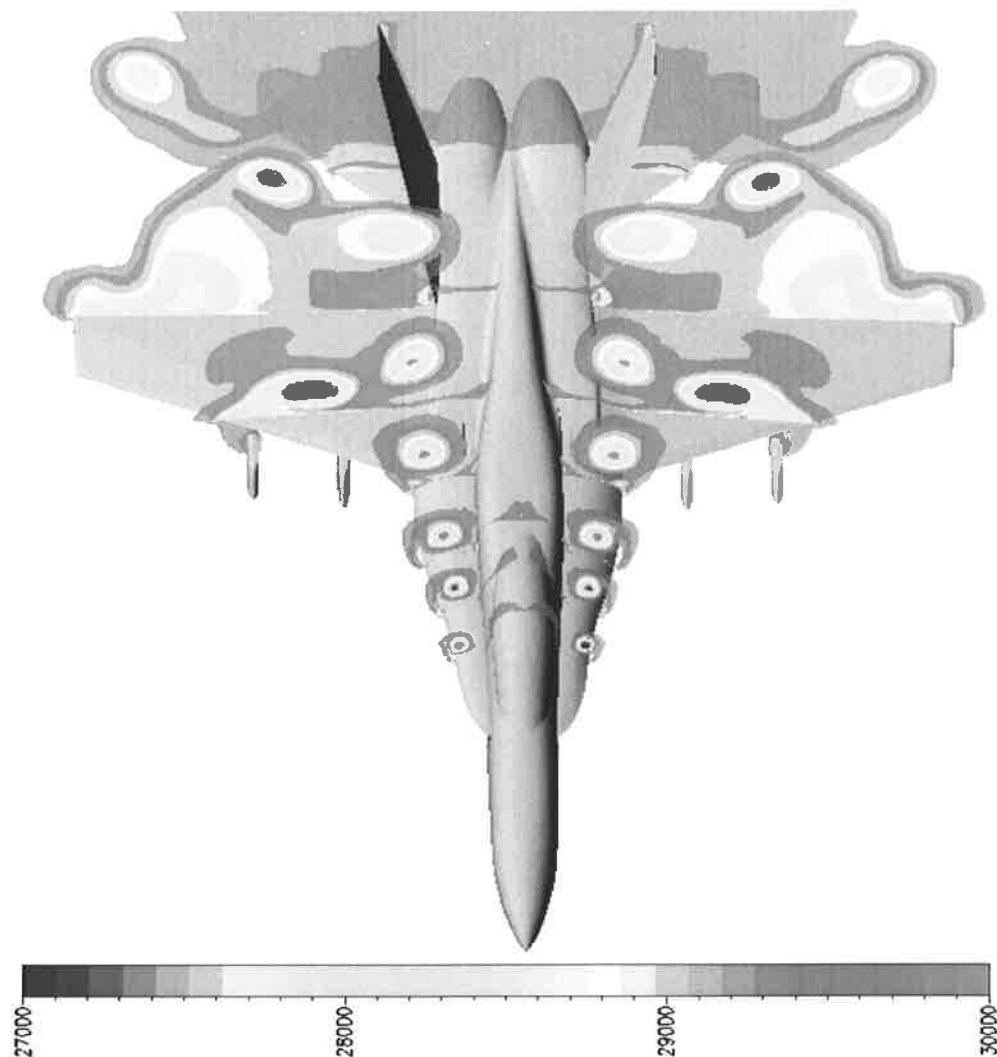
5:00 ~ 7:00
~~am~~
8:50 ~

Fig. 4. Total pressure contours on cross-flow planes at different longitudinal stations.

Another vortex is generated at the tip of the wing that trails downstream away from the vertical tail. As the vortical flow crosses the leading edge of the vertical tail, a smaller vortex develops at the root of the tail underneath the primary LEX vortex. The tail vortex exists totally at the outer surface of the vertical tail and it is rotating in the opposite direction to that of the primary LEX vortex.

The surface pressure coefficient on the upper and lower surfaces of the LEX at different fuselage stations (FS) at $\alpha = 30°$ are shown in Fig. 5. The results are compared with HARV flight-test data (Fisher et al., 1990) at three different FS. The spanwise coordinate is normalized by the span of the LEX at every FS, such that the normalized coordinate is zero at the leading edge of the LEX and one at the intersection with the fuselage. Two suction peaks are shown in the pressure distribution. The suction peaks correspond to the core of the primary and secondary LEX vortices, respectively. The pressure peaks and the positions of the vortex core of the primary vortex are accurately captured at all stations. However, the pressure peak of the secondary vortex at the aft position is overestimated. The figure shows the outboard motion of the core of the leading-edge vortices as the flow travels downstream. This is indicated form the outboard spanwise motion of the primary suction peak.

Three-dimensional and front view snapshots of the F/A-18 aircraft and the instantaneous streamlines of the LEX and wing vortices at four different angles of attack are shown in Fig. 6. The figure also shows the surface static pressure on the aircraft surfaces. The flow field at these high angles of attack is characterized by highly unsteady spiral flow, massive
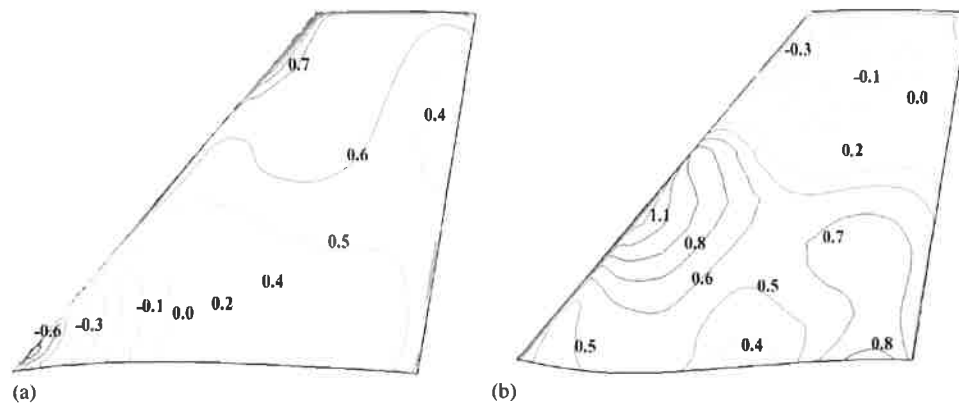
Fig. 9. Contour lines of pressure coefficient, $-C_p$, over the surfaces of the vertical tail. (a) Inboard surface; (b) outboard surface.
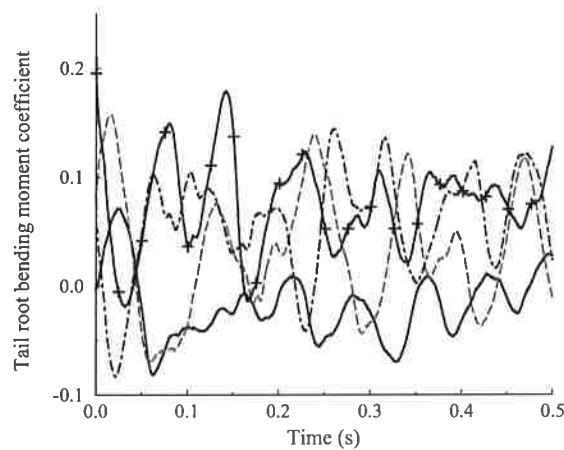

Fig. 10. The time history of the tail rbm coefficient: ——, $\alpha = 25°$; ---, $\alpha = 30°$; -·-, $\alpha = 35°$; +—+, $\alpha = 40°$.

James and Meyn (1994) used a 6×8 transducer array. James and Meyn (1994) showed that the density of the transducer array affects the integration of the buffet loads on the vertical tail. The results compare well with the experimental data over wide range of angles of attack. The maximum rbm occurs around the 30° angle of attack. That is when the vortex breakdown is completely ahead of the leading edge of the vertical tail. At higher angles of attack, the rbm decreases due to the diffusion of the vortex breakdown flow before it impinges upon the vertical tail. At low angles of attack ($\alpha < 25°$), there is still substantial amount of buffet. This buffet occurs even when the onset of vortex breakdown is downstream of the vertical tail. This observation suggests that the vortex breakdown may not be the only source of vertical tail buffeting of fighter aircraft. This was also observed experimentally by Gursul and Xie (1999). Several unsteady phenomena may contribute to the tail buffeting at lower angles of attack, such as vortex shedding, wakes from different parts of the aircraft, unsteady flow separation from the leading edge of the vertical tail (as observed in Fig. 4), and adverse feedback form the unsteady location of the onset of vortex breakdown.

4.3. Unsteady pressure at 45% chord and 60% span

Several publications have reported experimental and flight-test data at the 45% chord and 60% span point on the vertical tail. Thus, the unsteady pressure history at this point was monitored and analyzed for comparison. This would insure that results from different sources of tests and flight data have a common point for comparison. The time histories of the inboard, outboard, and differential unsteady pressure coefficients at the 45% chord and 60% span point are shown in Fig. 12. The figure indicates that the inboard surface of the tail experienced larger amplitude of fluctuation
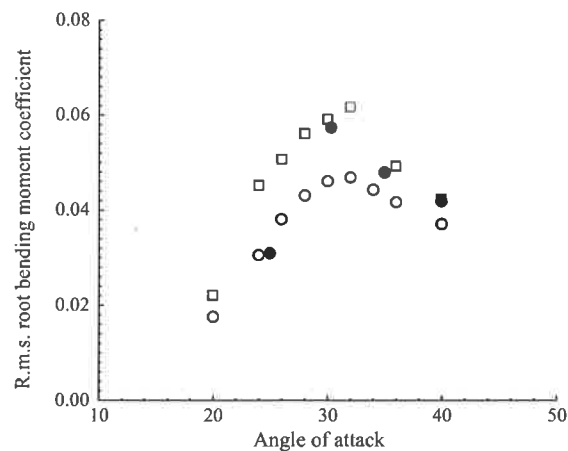
Fig. 11. RMS of tail rbm coefficient: O, full-scale model (James and Meyn, 1994); □, full-scale model (Pettit et al., 1994); ●, present computation.
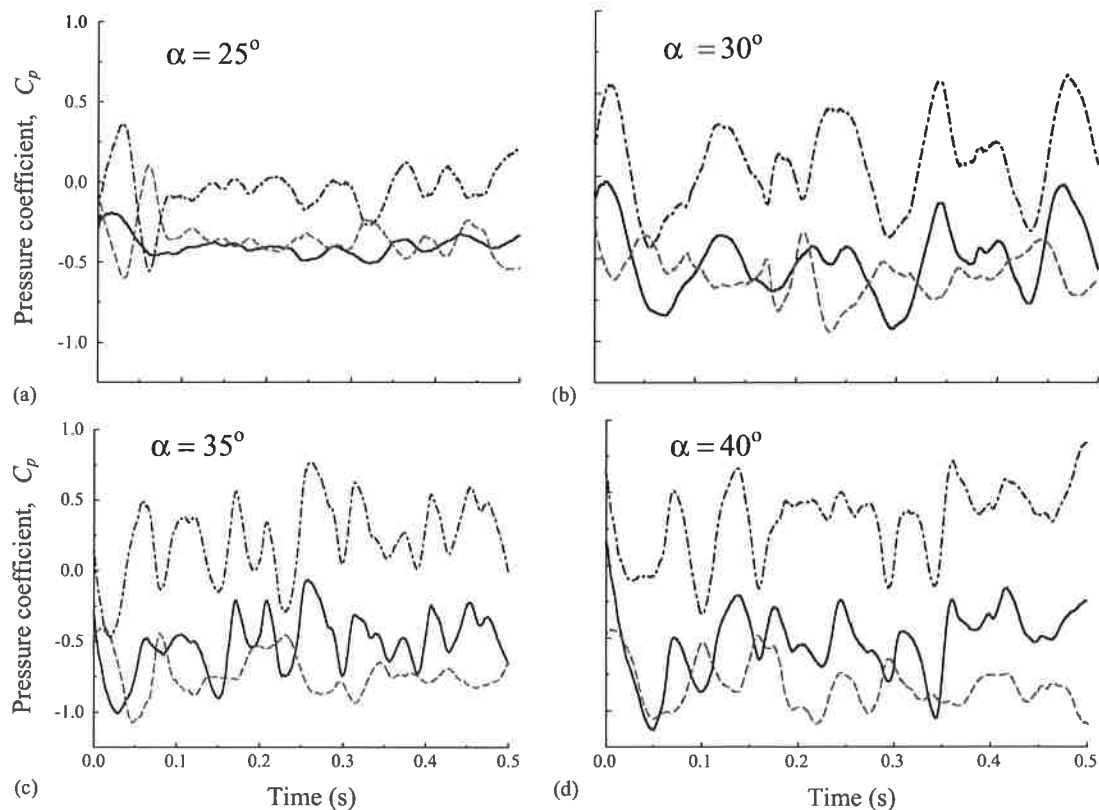

Fig. 12. The time histories of pressure coefficients on the vertical tail at 45% chord, 60% span: ——, inboard pressure; – – –, outboard pressure; – · –, differential pressure.

than the outboard surface, except at 25° angle of attack. This indicates that the inboard surface of the vertical tail has a more significant contribution in the unsteadiness of the problem than the outboard surface.

The r.m.s. of inboard, outboard and differential pressure coefficients are shown in Fig. 13. The results are compared with flight-test data, full-scale and 16%-scale wind-tunnel data of Meyn et al. (1994). The results compare well with the

High AOA problems.

- Wing rock: The delta wing exhibits a nonlinear roll moment behavior leading to a limit cycle oscillation.

$\emptyset$ ↑ limit cycle magnitude.
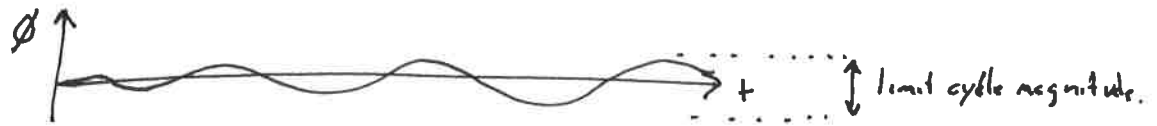
- Vortex interaction + Bursting
    F18 verticle tail

- Spins

- Non-linear Aerodynamics. coupled with Inertial coupling.
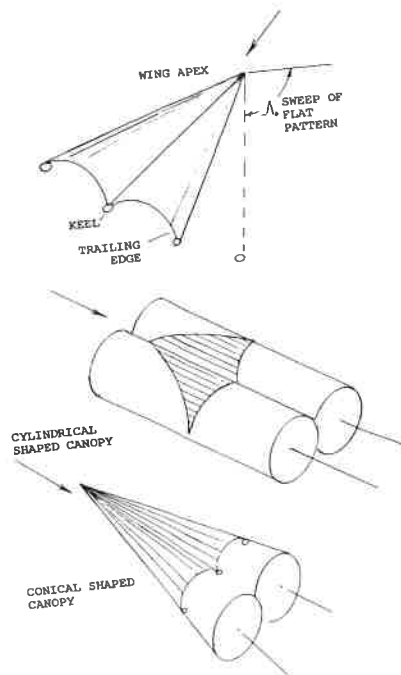
- High Drag

Rogallo / Parawings
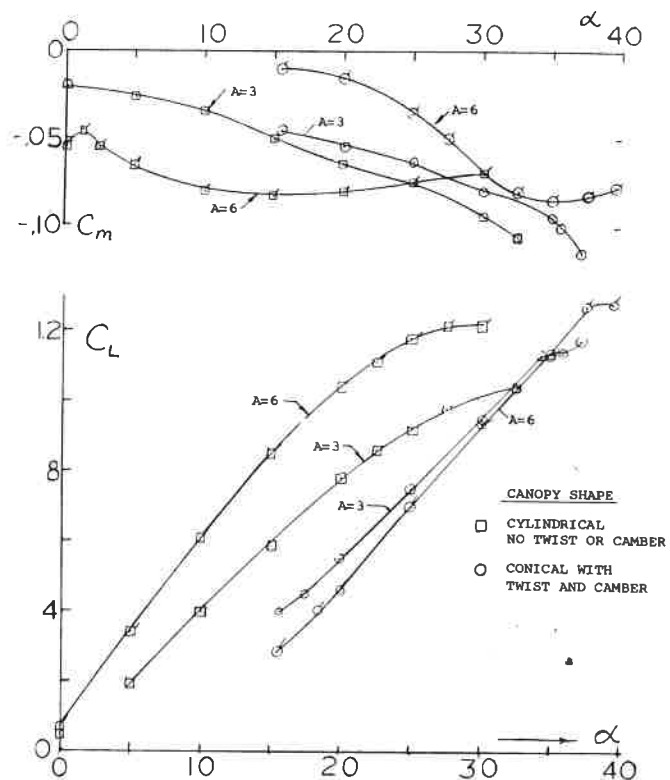

Figure 32. Geometry characteristics of parawings.

Figure 33. Lifting and moment characteristics of two-lobed parawings, A = 3 and 6.